J. Fluid Mech. (2013), *vol.* 737, *pp.* 205–231.
doi:10.1017/jfm.2013.559

Stability of columnar convection in a porous medium

Duncan R. Hewitt[1,†], **Jerome A. Neufeld**[1,2,3] **and John R. Lister**[1]

[1]Institute of Theoretical Geophysics, Department of Applied Mathematics and Theoretical Physics, University of Cambridge, Wilberforce Road, Cambridge CB3 0WA, UK

[2]Department of Earth Science, University of Cambridge, Cambridge CB2 3EQ, UK

[3]BP Institute, University of Cambridge, Cambridge CB3 0EZ, UK

(Received 28 May 2013; revised 23 August 2013; accepted 17 October 2013; first published online 22 November 2013)

Convection in a porous medium at high Rayleigh number Ra exhibits a striking quasisteady columnar structure with a well-defined and Ra-dependent horizontal scale. The mechanism that controls this scale is not currently understood. Motivated by this problem, the stability of a density-driven 'heat-exchanger' flow in a porous medium is investigated. The dimensionless flow comprises interleaving columns of horizontal wavenumber k and amplitude $\widehat{A}$ that are driven by a steady balance between vertical advection of a background linear density stratification and horizontal diffusion between the columns. Stability is governed by the parameter $A = \widehat{A}Ra/k$. A Floquet analysis of the linear-stability problem in an unbounded two-dimensional domain shows that the flow is always unstable, and that the marginal-stability curve is independent of A. The growth rate of the most unstable mode scales with $A^{4/9}$ for $A \gg 1$, and the corresponding perturbation takes the form of vertically propagating pulses on the background columns. The physical mechanism behind the instability is investigated by an asymptotic analysis of the linear-stability problem. Direct numerical simulations show that nonlinear evolution of the instability ultimately results in a reduction of the horizontal wavenumber of the background flow. The results of the stability analysis are applied to the columnar flow in a porous Rayleigh–Bénard (Rayleigh–Darcy) cell at high Ra, and a balance of the time scales for growth and propagation suggests that the flow is unstable for horizontal wavenumbers k greater than $k \sim Ra^{5/14}$ as $Ra \to \infty$. This stability criterion is consistent with hitherto unexplained numerical measurements of k in a Rayleigh–Darcy cell.

Key words: convection, convection in porous media, instability

1. Introduction

Convection in porous media plays an important role in a range of environmental and industrial processes (Nield & Bejan 2006), such as the extraction of geothermal energy by underground heating (Cheng 1978), the flow of saline groundwater driven by evaporation from the surface (Wooding *et al.* 1997), and the formation of freckles in alloy castings (Fowler 1985). More recently, there has been particular interest in

† Email address for correspondence: drh39@cam.ac.uk

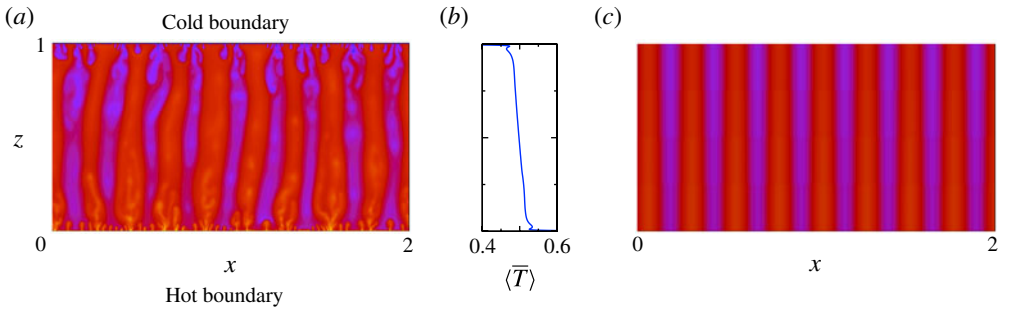

FIGURE 1. (Colour online) (*a*) A snapshot of the temperature field in a Rayleigh–Darcy (porous Rayleigh–Bénard) cell at $Ra = 2 \times 10^4$ (taken from Hewitt *et al.* 2012), which is dominated by vertical columnar exchange flow across the domain; (*b*) the corresponding temporally and horizontally averaged temperature $\langle \overline{T} \rangle(z)$, which shows the relatively weak linear temperature gradient across the interior of the domain; and (*c*) the temperature field of steady heat-exchanger flow with the same wavelength and background temperature gradient as (*a*).

the effect of convective transport on the long-term storage of CO_2 by geological sequestration (Orr 2009), which has been widely proposed as a means of stabilizing the rising concentration of atmospheric CO_2 (Metz *et al.* 2005).

The structure of convection depends on the relative strength of advection and diffusion, as described by the Rayleigh number *Ra*. Although the detailed form of the flow depends on the geometry of the system, convective flow in a porous medium at high *Ra* is typically dominated by long-lasting columnar plumes. Such plumes are a generic feature of both transient and statistically steady convection at high *Ra* (Hewitt, Neufeld & Lister 2013). An archetypal example of this columnar structure is provided by the flow in a two-dimensional porous Rayleigh–Bénard cell (figure 1*a*). For the rest of this paper, to avoid confusion with the pure fluid Rayleigh–Bénard cell, we will refer to this porous cell as a Rayleigh–Darcy cell.

The Rayleigh–Darcy cell has lower and upper boundaries held at fixed hot and cold temperatures, respectively, and thus attains a statistically steady state, which allows for accurate characterization of the convective dynamics. For $Ra < 4\pi^2$, there is no convection (Lapwood 1948), while for $4\pi^2 < Ra \lesssim 1300$, the flow exhibits convective rolls, which undergo a series of bifurcations that perturb the background flow as *Ra* is increased (Graham & Steen 1994). For $Ra \gtrsim 1300$, the rolls are completely broken down by the growth of destabilizing plumes from the upper and lower boundaries, and there is a dramatic transition in the dynamical structure. The flow becomes dominated by persistent vertical columnar-exchange flow across the interior of the domain, driven by chaotic mixing of small 'proto-plumes' at the upper and lower boundaries (Otero *et al.* 2004; Hewitt, Neufeld & Lister 2012). Curiously, it appears that the columnar flow not only persists, but becomes increasingly well organized as *Ra* increases. This behaviour is quite unlike the disordered turbulent dynamics encountered in a pure fluid Rayleigh–Bénard cell at high *Ra* (e.g. Ahlers, Grossmann & Lohse 2009). Hewitt *et al.* (2012) found that, as *Ra* increases, the interior columnar flow becomes increasingly well described by a steady 'heat-exchanger' solution, in which vertical advection of a background temperature gradient exactly balances horizontal diffusion (figure 1). We note that the interior background gradient is much weaker than a steady conduction gradient, as most of the temperature contrast across the domain is taken up in the

diffusive boundary layers. Numerical measurements by Hewitt *et al.* (2012) over the range $1300 < Ra \leqslant 4 \times 10^4$ gave an approximate scaling for the wavenumber k of the columnar flow of $k \sim Ra^{0.4}$, although they pointed out that there was some suggestion of a slightly smaller exponent asymptotically. While k clearly increases with Ra, the amplitude of the columnar flow tends towards a constant, consistent with an asymptotic Nusselt-number scaling $Nu \sim Ra$.

Columnar structures are also very widely observed in two- and three-dimensional convective flow driven by a source of buoyancy on one boundary only. Following the onset of convection, flow below a dense source (or, equivalently, above a buoyant source) is marked by vigorous mixing at the boundary which feeds into persistent downwelling plumes, as observed in several experimental (Neufeld *et al.* 2010; Backhaus, Turitsyn & Ecke 2011; Slim *et al.* 2013) and numerical (Pau *et al.* 2010; Hidalgo *et al.* 2012; Fu, Cueto-Felgueroso & Juanes 2013) studies. If the boundaries of the domain are impermeable then, over longer times, the convective flow weakens as the density in the interior increases towards that of the upper boundary. This 'shutdown' regime was studied by Hewitt *et al.* (2013), who found that the columnar flow across the interior of the domain persisted throughout, with a wavenumber k that decreased slowly as the average interior density increased and the effective Rayleigh number decreased. The relationship between $k(t)$ and $Ra(t)$ was in excellent quantitative agreement with results from the Rayleigh–Darcy cell discussed above.

The physical mechanism that governs the wavenumber $k(Ra)$ has so far remained elusive. Hewitt *et al.* (2012) argued that k is not controlled directly by the small-scale dynamics of proto-plumes near the boundary, since these have a lateral scale of Ra^{-1}, which is a much stronger dependence on Ra than the observed wavenumber exponent of $\sim$0.4. It has been suggested by Wen *et al.* (2012, 2013) that the wavenumber is determined by the size of a 'minimal flow unit', which is set by the largest wavenumber k for which the buoyancy flux remains independent of k. Solutions for steady convective flow in a narrow Rayleigh–Darcy cell (Corson 2011) give a scaling of $k \sim Ra^{1/2}$ for the minimal flow unit, while recent numerical measurements of the minimal flow unit for unsteady flow suggest a slightly weaker dependence on Ra (Wen *et al.* 2013), in rough agreement with the observed wavenumber scaling of $Ra \sim k^{0.4}$. This observation does not, however, provide a mechanism for the physical control of wavenumber. The aim of this paper is to explore whether the wavenumber might be determined by the stability of the columnar flow.

Columnar 'heat-exchanger' flows are not only observed in porous media; similar flow is found in double-diffusive systems, in the form of 'salt fingers'. These fingers can occur when the density is a function of two components with different molecular diffusivities, such as heat and salt, provided that the unstably distributed component (salt) has a lower diffusivity than the stably distributed component (heat) (Huppert & Turner 1981). Stability of the salt fingers has long been suggested as the controlling mechanism for their dynamical structure (Stern 1969); it was explored in detail by Holyer (1981, 1984), and remains an active area of study (Radko & Smith 2012). The Floquet analysis employed by Holyer (1984) to solve the linear-stability problem provides a starting point for our approach here.

In this paper, we examine the stability of two-dimensional columnar heat-exchanger flow in a porous medium. The flow is driven by temperature differences between the columns, but the analysis is equally applicable to compositional convection. In § 2, we set out the governing equations for heat-exchanger flow in an unbounded medium, and find that the flow is controlled by a single parameter, the rescaled amplitude A. In § 3, we use Floquet theory to perform a linear-stability analysis of this flow. We show

that the dominant instability for $A \gtrsim 17.2$ has double the horizontal wavelength of the background columns and a relatively small vertical wavenumber, and we determine the dependence on A of the vertical wavenumber and growth rate of this mode. In § 4, we present an asymptotic analysis of the most unstable perturbation for $A \gg 1$, and discuss the physical mechanism of instability. In § 5, we explore the nonlinear evolution of the instability for large A using direct numerical simulations.

In § 6, we discuss the relevance of all these results for the scaling of the columnar wavenumber k in a Rayleigh–Darcy cell at high Ra. A balance of the time scale for instability and the time scale for advection of perturbations across the domain suggests that the columnar flow should be unstable for wavenumbers $k \sim Ra^{5/14}$ as $Ra \to \infty$, while a correction to this asymptotic estimate gives a slightly stronger dependence on Ra for $Ra < O(10^5)$. These scalings give good agreement with numerical measurements of the dominant wavenumber k from the interior of a Rayleigh–Darcy cell.

We conclude with a summary of the main results and their implications in § 7.

2. Governing equations

2.1. *Dimensionless equations*

We consider flow in a homogeneous, isotropic and unbounded two-dimensional porous medium, with horizontal and vertical coordinates x and z, respectively. The flow $\boldsymbol{u} = (u, w)$ is incompressible and satisfies Darcy's law. The density ρ of the fluid is linearly related to the temperature T, which satisfies a transport equation. These equations are given in dimensionless variables by

$$\boldsymbol{\nabla} \cdot \boldsymbol{u} = 0, \quad \boldsymbol{u} = -(\boldsymbol{\nabla} p + \rho \hat{\boldsymbol{z}}), \tag{2.1a,b}$$

$$\rho = 1 - T, \quad \frac{\partial T}{\partial t} + \boldsymbol{u} \cdot \boldsymbol{\nabla} T = \frac{1}{Ra} \nabla^2 T, \tag{2.2a,b}$$

where p is the pressure. The Rayleigh number Ra, which can be thought of as the ratio of diffusive and convective time scales over a distance H, is given by

$$Ra = \frac{\rho_0 \beta \, \Delta T \, g \Pi H}{\phi D \mu}, \tag{2.3}$$

where Π is the permeability, ϕ is the porosity, g is the gravitational acceleration, ρ_0 is a reference density, β is the coefficient of thermal expansion, D is the effective thermal diffusivity and μ is the viscosity of the fluid, all of which are assumed to be constant. We have assumed that there is negligible heat transfer to the solid phase of the medium and, as such, these equations are equally applicable to compositional convection. We have non-dimensionalized with respect to a temperature scale ΔT, which determines the buoyancy–velocity scale $U = \rho_0 \beta \, \Delta T g \Pi / \mu$, and with respect to a length scale H, which determines the convective time scale $\phi H / U$. In the case of a Rayleigh–Darcy cell, these scales would correspond to the driving temperature difference across the domain and the height of the domain, respectively. We note that, with this choice of dimensionless variables, the Rayleigh number takes the role of an inverse diffusivity in (2.2).

We satisfy (2.1*a*) by introducing a streamfunction ψ, where $(u, w) = (\partial \psi / \partial z, -\partial \psi / \partial x)$. We take the curl of (2.1*b*) to eliminate the pressure, and combine

with the equation of state (2.2*a*) to obtain

$$\nabla^2\psi = -\frac{\partial T}{\partial x}. \tag{2.4}$$

Equations (2.2*b*) and (2.4) govern the flow.

There is an exact solution of (2.2*b*) and (2.4) given by a steady 'heat-exchanger' flow (Hewitt *et al.* 2012), in which vertical advection of a background linear temperature gradient by interleaving columns of exchange flow balances horizontal diffusion between the columns; the horizontal velocity is zero and the vertical velocity is directly proportional to the sinusoidal variation of temperature across the columns. The heat-exchanger solution $[\psi_0, T_0]$ is characterized by a wavenumber k and amplitude $\widehat{A}$, and is given by

$$T_0 = \widehat{A}\cos kx - \frac{k^2}{Ra}z, \quad \psi_0 = -\frac{\widehat{A}}{k}\sin kx, \quad u_0 = 0, \quad w_0 = \widehat{A}\cos kx, \tag{2.5a,b,c,d}$$

where $u_0 = \partial\psi_0/\partial z$ and $w_0 = -\partial\psi_0/\partial x$ are the corresponding horizontal and vertical velocity of the flow. The average vertical advective heat flux for heat-exchanger flow scales with $\widehat{A}^2$, and is independent of the wavenumber k.

2.2. *Rescaled equations*

The heat-exchanger flow (2.5) is governed by three parameters k, $\widehat{A}$ and Ra, which describe the wavenumber, the amplitude and the relative strength of advection and diffusion, respectively. We can scale out two of these apparent degrees of freedom by setting

$$\boldsymbol{X} = k\boldsymbol{x}; \quad \Theta = \frac{Ra}{k}T; \quad \Psi = Ra\,\psi; \quad \tau = \frac{k^2}{Ra}t. \tag{2.6}$$

The governing equations (2.4) and (2.2*b*) become

$$\nabla^2\Psi = -\frac{\partial\Theta}{\partial X}, \quad \frac{\partial\Theta}{\partial\tau} + \frac{\partial\Psi}{\partial Z}\frac{\partial\Theta}{\partial X} - \frac{\partial\Psi}{\partial X}\frac{\partial\Theta}{\partial Z} = \nabla^2\Theta, \tag{2.7a,b}$$

and the heat-exchanger solution (2.5) becomes

$$\Theta_0 = A\cos X - Z, \quad \Psi_0 = -A\sin X, \quad U_0 = 0, \quad W_0 = A\cos X. \tag{2.8a,b,c,d}$$

The rescaled strength of the flow

$$A = \frac{\widehat{A}Ra}{k}, \tag{2.9}$$

is now the only free parameter. Equation (2.8) gives the background flow for the stability analysis of the subsequent sections of this paper.

3. Linear-stability analysis

3.1. *Theory*

We consider small perturbations $[\widetilde{\Psi}, \widetilde{\Theta}]$ to the background heat-exchanger flow of the form

$$\widetilde{\Psi} = \mathrm{Re}\left\{F(X)\exp\left(\sigma t + \mathrm{i}\alpha Z\right)\right\}, \quad \widetilde{\Theta} = \mathrm{Re}\left\{G(X)\exp\left(\sigma t + \mathrm{i}\alpha Z\right)\right\}, \tag{3.1a,b}$$

where $|F|, |G| \ll 1$. By retaining only terms that are linear in F and G, the governing equations (2.7) become

$$F'' - \alpha^2 F = -G', \quad (\sigma + \mathrm{i}\alpha A \cos X)\, G + F' - \mathrm{i}\alpha A \sin X F = G'' - \alpha^2 G. \quad (3.2a,b)$$

Owing to the spatial dependence of the coefficients in (3.2*b*), we cannot assume a simple-harmonic normal-mode form for F and G. Instead, we utilize the periodicity of the equations: the coefficients are periodic in X with period 2π, and, therefore, (3.2) forms a Floquet system. Floquet theory (see Jordan & Smith 1999, for example) implies that the eigenmodes $\boldsymbol{y}_j(X)$ of any homogeneous system of linear ordinary differential equations that has periodic coefficients with period λ can be written in the form $\boldsymbol{y}_j(X) = \boldsymbol{p}_j(X)\exp(\mathrm{i}\beta_j X)$, where $\boldsymbol{p}_j$ is periodic with period λ, and β_j is a (possibly complex) constant. If the eigenmodes are also required to be spatially periodic, then β_j must be real. In (3.2), $\lambda = 2\pi$, and so the function $\boldsymbol{p}_j(X)$ can be written as a sum of complex exponentials of the form $\exp(\mathrm{i}nX)$ for integer n (Beaumont 1981). We therefore look for spatially periodic eigenmodes of the form

$$\begin{pmatrix} F \\ G \end{pmatrix} = \mathrm{Re}\left\{ \exp(\mathrm{i}\beta X) \sum_{n=-\infty}^{\infty} \begin{pmatrix} F_n \\ G_n \end{pmatrix} \exp(\mathrm{i}nX) \right\}, \quad (3.3)$$

where β is real. Owing to the invariance of (3.3) under integer shifts in β and under reflection $\beta \to -\beta$, we can pick $0 \leqslant \beta \leqslant 1/2$ without loss of generality. We refer to β as the horizontal wavenumber of the perturbation; strictly, β is the wavenumber of the largest horizontal scale, and the infinite sum allows for perturbations on smaller scales.

The eigenvalue σ is given as a function of α and β by substituting the Fourier sum (3.3) into (3.2) and rewriting $\sin X$ and $\cos X$ in terms of complex exponentials. Equation (3.2) becomes

$$\mathrm{i}\gamma_n^2 F_n = -(\beta + n) G_n, \quad (3.4a)$$

$$\mathrm{i}(\beta + n) F_n - \frac{\alpha A}{2}(F_{n-1} - F_{n+1}) = -\left(\gamma_n^2 + \sigma\right) G_n - \frac{\mathrm{i}\alpha A}{2}(G_{n-1} + G_{n+1}), \quad (3.4b)$$

where $\gamma_n^2 = (\beta + n)^2 + \alpha^2$, and eliminating F between (3.4*a*) and (3.4*b*) gives

$$\left[\frac{(\beta + n)^2}{\gamma_n^2} - \gamma_n^2 - \sigma\right] G_n = \frac{\mathrm{i}\alpha A}{2}\left[\left(1 + \frac{\beta + n + 1}{\gamma_{n+1}^2}\right) G_{n+1} + \left(1 - \frac{\beta + n - 1}{\gamma_{n-1}^2}\right) G_{n-1}\right]. \quad (3.5)$$

Equation (3.5) can be written as an infinite matrix equation of the form

$$\boldsymbol{M}\boldsymbol{G} = \sigma \boldsymbol{G}, \quad (3.6)$$

where the vector $\boldsymbol{G} = (\ldots G_{n-1}, G_n, G_{n+1}, \ldots)$, and $\boldsymbol{M}$ is an infinite (tridiagonal) matrix. Solutions to (3.6) are found by looking for eigenvectors $\boldsymbol{G}$ of $\boldsymbol{M}$ with eigenvalues σ. The real part of σ gives the growth rate of perturbations.

3.2. *Solutions*

3.2.1. *The limit of large horizontal scales*

The equations simplify dramatically if we only consider perturbations on the largest horizontal scales, which is achieved by severely truncating the infinite sum in (3.3) such that $G_n = 0$ for all $n \neq 0$. In this long-wavelength limit, the columnar flow is completely decoupled from the perturbation, which is equivalent to setting $A = 0$ and

losing the effect of flow on stability. Equation (3.5) reduces to the standard linear-stability analysis of a linear background temperature field about rest (Nield & Bejan 2006), and the growth rate is given by the usual Rayleigh modes,

$$\sigma = \frac{\beta^2}{\beta^2 + \alpha^2} - \left(\beta^2 + \alpha^2\right). \tag{3.7}$$

The flow is unstable if $\beta > \beta^2 + \alpha^2$. If there is no constraint on the size of the domain, then the growth rate is maximized by $\alpha \ll \beta \ll 1$, which gives a limiting growth rate $\mathrm{Re}\{\sigma\} = 1$. If the perturbation is constrained in a finite domain, then the instability takes the form of one or more large convective rolls.

3.2.2. *Numerical solutions that incorporate smaller scales*

We incorporated the effects of smaller horizontal modes on the stability of the flow by retaining more terms in the Fourier sum in (3.3) and solving (3.6) numerically. We found eigenvalues σ by truncating the infinite sum in (3.6) to $-N \leqslant n \leqslant N$, for some integer $N(\alpha, \beta, A)$, which was increased until the relative error in the eigenvalue with the largest real part (growth rate) was less than 10^{-5}. We denote the eigenvalue with the largest real part $\hat{\sigma}(\alpha, \beta, A)$.

Figure 2 shows contour plots of the growth rate $\mathrm{Re}\{\hat{\sigma}\}$ against the vertical and horizontal wavenumbers α and β, for different values of A. For all A, we find that the growth rate is negative for $\alpha > 1/2$, and this range is therefore not shown. We also recall that we only need to consider values of β in the range $0 \leqslant \beta \leqslant 1/2$ due to the symmetries of the system.

Figure 2 reveals three interesting features. First, the marginal-stability curve $\mathrm{Re}\{\hat{\sigma}\} = 0$ appears to be independent of the amplitude A. This observation is confirmed analytically in § 3.2.3. Second, for $A \lesssim 17.2$, the most unstable mode occurs at $\alpha = \beta = 0$ and has constant growth rate $\mathrm{Re}\{\hat{\sigma}\} = 1$, which is the same as the case $A = 0$ discussed above in § 3.2.1. Third, a new mode with $\beta = 1/2$ and $\alpha > 0$ becomes increasingly unstable as A is increased, and, for $A \gtrsim 17.2$ (figure 2*c,d*), the new mode has a growth rate that exceeds that of the zero-wavenumber mode. For all higher values of A, this mode is the most unstable.

The most unstable mode is defined by the wavenumbers $(\alpha_M(A), \beta_M(A))$ that maximize the growth rate $\mathrm{Re}\{\hat{\sigma}(\alpha, \beta, A)\}$ over α and β. We label the most unstable mode as $\sigma_M(A) = \hat{\sigma}(\alpha_M, \beta_M, A)$, and the corresponding cut-off value for convergence of the Fourier sum in (3.3) as $N_M(A) = N(\alpha_M, \beta_M, A)$.

The maximum growth rate $\mathrm{Re}\{\sigma_M\}$ and the phase speed $c_M = -\mathrm{Im}\{\sigma_M\}/\alpha_M$ are shown in figure 3. The change in the most unstable mode at $A \approx 17.2$ can be observed as the point where the maximum growth rate begins to increase and the phase speed becomes non-zero. Both $\mathrm{Re}\{\sigma_M\}$ and $|c_M|$ show an asymptotic power-law dependence on A, which is very well fitted by

$$\mathrm{Re}\{\sigma_M\} = 0.231A^{4/9}, \quad c_M = \pm A \quad \text{as } A \to \infty. \tag{3.8a,b}$$

The most unstable mode, therefore, propagates at the maximum speed of the background flow, either up or down depending on the alignment of the perturbation (see § 3.2.4 below). (In fact, we find that the magnitude of the phase speed for all unstable modes with $\alpha > 0$ is asymptotically given by A, while that of the stable modes is zero.)

The wavenumbers of the most unstable mode are both zero for $A \lesssim 17.2$. At $A \approx 17.2$, the vertical wavenumber α_M becomes non-zero, and gradually decreases

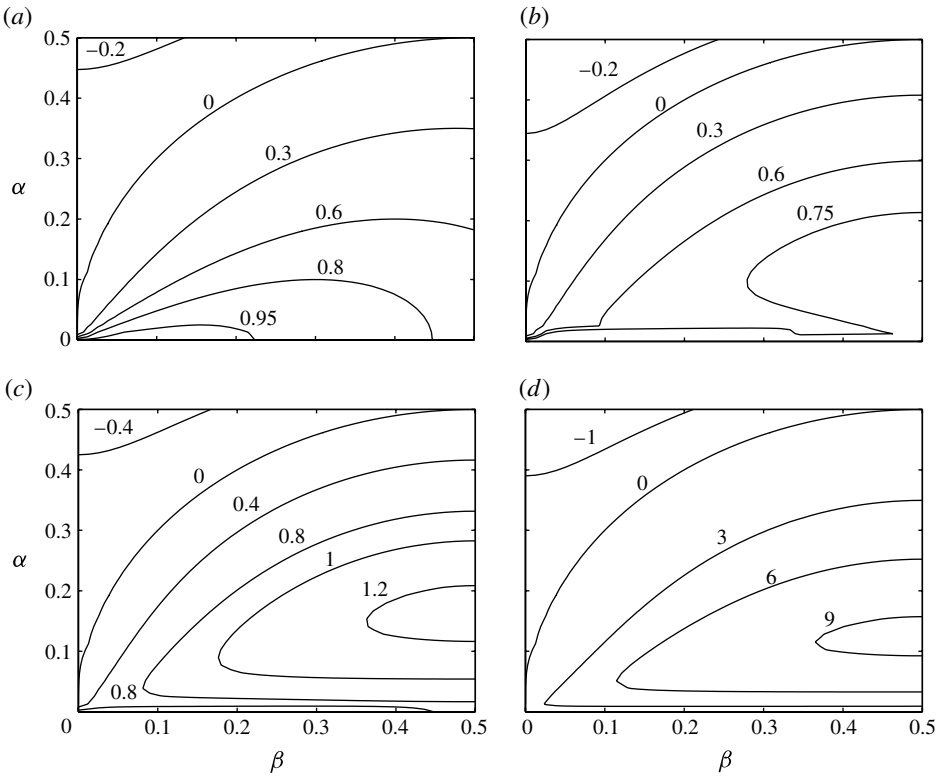

FIGURE 2. Contours of the growth rate $\mathrm{Re}\{\hat{\sigma}\}$ (as marked) against the horizontal wavenumber β and the vertical wavenumber α at amplitudes: (*a*) $A = 0$; (*b*) $A = 2^3$; (*c*) $A = 2^5$; and (*d*) $A = 2^{12}$. The marginal-stability curve is independent of A (§ 3.2.3). The maximum growth rate is initially $\mathrm{Re}\{\hat{\sigma}\} = 1$, which is attained at $\alpha = \beta = 0$. As A increases, a mode with horizontal wavenumber $\beta = 0.5$ and $\alpha > 0$ becomes increasingly unstable. For $A \gtrsim 17.2$ (*c*,*d*), this mode has a growth rate that is greater than 1.

as A increases further (figure 4*a*). Asymptotically, α_M is very well fitted by

$$\alpha_M = 0.332A^{-1/9} \quad \text{as } A \to \infty. \tag{3.9}$$

The corresponding horizontal wavenumber β_M is 1/2 for all $A \gtrsim 17.2$, as suggested by the results of figure 2, which means that the most unstable perturbation has twice the wavelength of the background flow.

The cut-off value $N_M = N(\alpha_M, \beta_M, A)$ increases like $A^{2/9}$ for large A (figure 4*b*). Since larger wavenumbers in the Fourier sum in (3.3) describe shorter horizontal scales, the need to increase N_M for convergence suggests that the smallest horizontal scales of the most unstable perturbation decrease like

$$N_M^{-1} \sim A^{-2/9} \quad \text{as } A \to \infty. \tag{3.10}$$

In § 4, we confirm that the truncated Fourier sum remains an accurate representation of the solution by comparison with an asymptotic expansion of the differential equations (3.2).

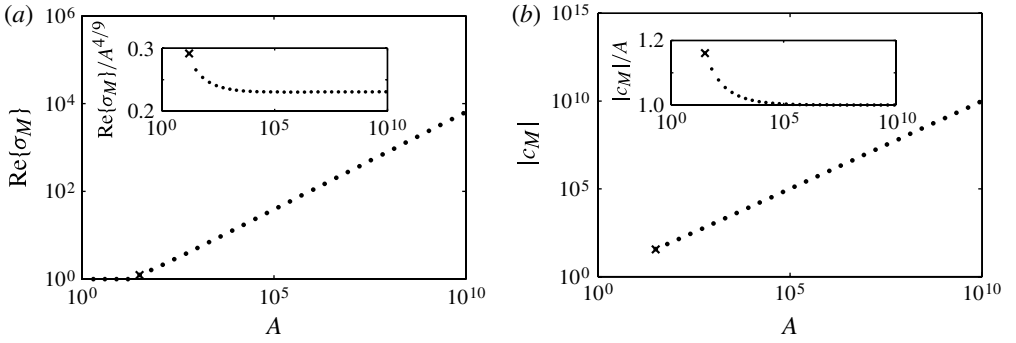

FIGURE 3. (*a*) The maximum growth rate $\mathrm{Re}\{\sigma_M\}$, which asymptotically scales like $A^{4/9}$ as shown in the inset, and (*b*) the magnitude of the corresponding phase speed $c_M = -\mathrm{Im}\{\sigma_M\}/\alpha_M$, which tends to the maximum background velocity A asymptotically, as shown in the inset. The cross signifies the first data point after the change of most unstable mode at $A \approx 17.2$.

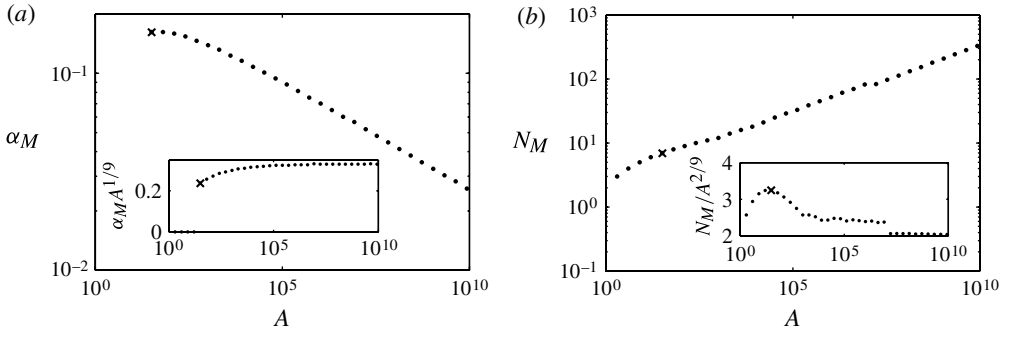

FIGURE 4. (*a*) The vertical wavenumber α_M of the most unstable mode, which asymptotically scales like $A^{-1/9}$ as shown in the inset, and (*b*) the cut-off $N_M = N(\alpha_M, \beta_M, A)$ for the Fourier sum in (3.3), which asymptotically scales like $A^{2/9}$ as shown in the inset. The origin of the discontinuity at $A \approx 10^7$ is unclear. The cross signifies the first data point after the change of most unstable mode at $A \approx 17.2$.

3.2.3. *Marginal stability*

The results of figure 2 suggest that the marginal-stability curve is independent of the amplitude A. Here we verify this suggestion analytically.

Marginal stability occurs when $\mathrm{Re}\{\hat{\sigma}\} = 0$. Numerical results for general $A > 0$ suggest that the eigenvector $\boldsymbol{G}$ corresponding to the marginally stable modes takes the simple form $G_{-1} = \pm G_0$, and $G_n = 0$ for $n \neq 0, -1$. Motivated by this observation, and the corresponding form of F_n from (3.4*a*), we consider eigenvectors $[F, G]$ of the form

$$F = \pm\left[\sin\beta X + \sin(1-\beta)X\right], \quad G = \mp\left[\cos\beta X + \cos(1-\beta)X\right]. \quad (3.11a,b)$$

On substituting (3.11) into the advection–diffusion equation (3.2*b*), we obtain

$$\left[\sigma + \left(\beta^2 + \alpha^2 - \beta\right)\right] G = \mathrm{i}\alpha A\left[\sin XF - \cos XG\right], \quad (3.12)$$

which, by using double-angle formulae and (3.11), reduces to

$$\left[\sigma + \left(\beta^2 + \alpha^2 - \beta\right)\right] = \pm \mathrm{i}\alpha A. \tag{3.13}$$

The eigenfunctions (3.11) must also satisfy Poisson's equation (3.2*a*); this gives the requirement that

$$\beta = \beta^2 + \alpha^2, \tag{3.14}$$

which is precisely the marginal-stability relationship for $A = 0$ given in (3.7). Combining (3.13) and (3.14) gives

$$\sigma = \pm \mathrm{i}\alpha A, \tag{3.15}$$

which corresponds to a phase speed of $|c| = A$ and a growth rate of zero.

The marginal-stability curve (3.14) is, therefore, independent of A, as are the corresponding eigenfunctions $[F, G]$ (3.11), provided that $A > 0$. Interestingly, the eigenfunctions do differ from those for $A = 0$, which are pure Fourier modes with wavenumber β; the presence of background flow with unit wavenumber introduces an additional component to the marginally stable perturbation with wavenumber $1 - \beta$.

3.2.4. *Structure of the most unstable perturbation*

For $A \lesssim 17.2$, the most unstable mode has $\alpha_M = \beta_M = 0$, growth rate $\mathrm{Re}\{\sigma_M\} = 1$ and phase speed $c_M = 0$. The instability takes the form of a roll-like perturbation of the background temperature gradient, with a wavelength that is independent of the background columnar flow. At $A \approx 17.2$, a different mode becomes the most unstable, which has half the horizontal wavenumber of the background flow $\beta_M = 1/2$. The vertical wavenumber and phase speed of this mode are also both non-zero.

Figure 5 shows the structure of the most unstable mode for $A = 2^5 = 32$ (figure 5*a,c*) and $A = 2^{20} \approx 10^6$ (figure 5*b,d*). The perturbation takes the form of tall, thin, counter-rotating rolls (figure 5*a,b*; right-hand plots). Each roll has width 2π, and is centred on a downwelling of the background columnar flow. The whole perturbation has horizontal period 4π. The temperature perturbation $\widetilde{\Theta}$ takes the form of claw-shaped pulses centred on the upwellings of the background flow (figure 5*a*; left-hand plot), which, for larger amplitudes (figure 5*b*; left-hand plot), split into two neighbouring pulses of the same sign.

The vertical velocity $\widetilde{W}$ and temperature $\widetilde{\Theta}$ of the dominant perturbation (figure 5*c,d*) are symmetric about $X = 2n\pi$ for integer n, and are almost indistinguishable from each other. As A increases, the profiles of $\widetilde{\Theta}$ and $\widetilde{W}$ become increasingly sinusoidal in the intervals $(2n\pi, 2(n+1)\pi)$, but their gradients change by an $O(1)$ amount through increasingly narrow regions centred on $X = 2n\pi$. The horizontal velocity $\widetilde{U}$ either diverges away from or converges into these regions.

The perturbations shown in figure 5 have a phase speed $c_M = A$ to leading order, and thus move upwards at the maximum speed of the background flow. If the perturbation were shifted horizontally by π, the pulses would be centred on the downwellings of the background flow and the phase speed would be $c_M = -A$; the growth rate and vertical wavenumber would be unchanged.

4. Asymptotic analysis of linear stability for $A \gg 1$

Motivated by the structure of the most unstable perturbation as just described, and in order to understand the physical balances behind the instability, we examine the linear stability of heat-exchanger flow in the asymptotic limit $A \gg 1$. In this limit,

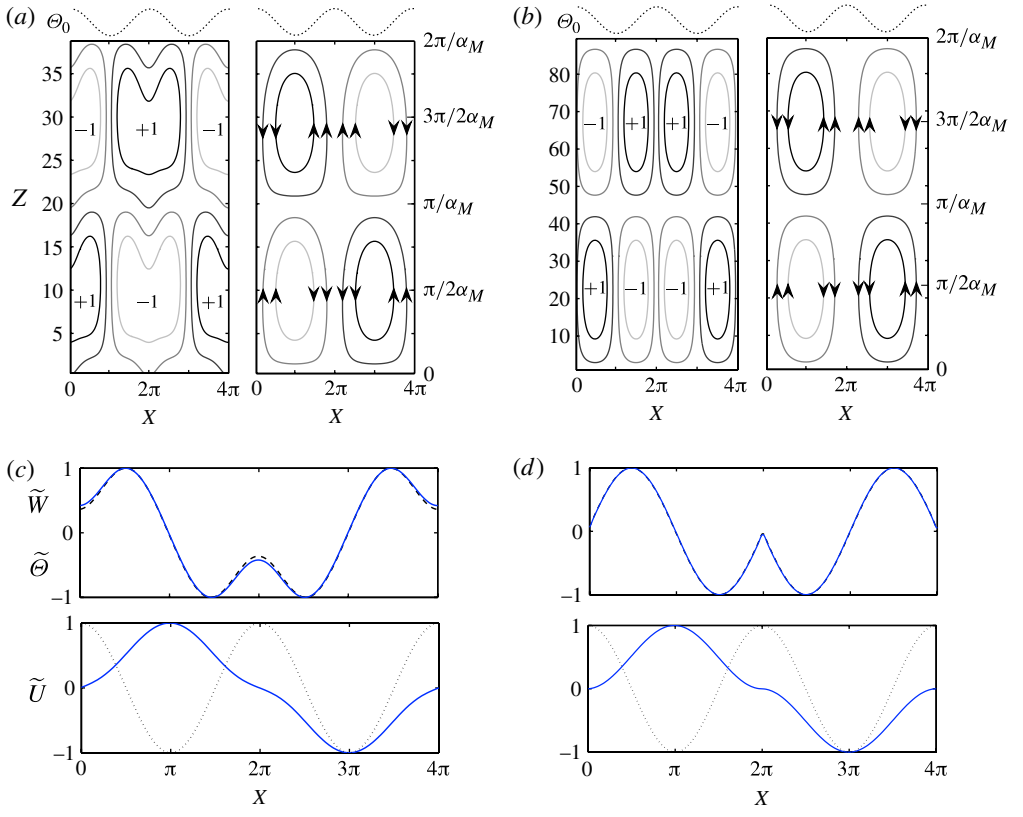

FIGURE 5. The structure of the most unstable perturbation (*a,c*) for $A = 2^5$ and (*b,d*) for $A = 2^{20}$. (*a,b*) Contours of the perturbation temperature $\widetilde{\Theta}$ (left) (scaled to unit amplitude), at intervals of 0.4, and streamlines (right) with arrows showing the direction of the flow, together with schematic profiles of the background flow $\Theta_0 = W_0$ (top). The perturbation is doubly periodic, with horizontal period 4π and vertical period $2\pi/\alpha_M$. (*c,d*) Horizontal profiles of the perturbation quantities (scaled to unit amplitude): upper plots show the temperature $\widetilde{\Theta}$ (solid) and vertical velocity $\widetilde{W} = -\partial\widetilde{\Psi}/\partial X$ (dashed) at $Z = \pi/2\alpha_M$; lower plots show the horizontal velocity $\widetilde{U} = \partial\widetilde{\Psi}/\partial Z$ (solid) at $Z = \pi/\alpha_M$ together with the background columnar flow Θ_0 (dotted) scaled by A. The vertical velocity and temperature perturbations are almost indistinguishable. The perturbations shown here propagate upwards; the same perturbations shifted horizontally by π would propagate downwards and have the same growth rate.

the dominant balance in the advection–diffusion equation (3.2*b*) is most obviously between horizontal advection of the background temperature by the perturbation $\sim\alpha A \sin XF$ and vertical advection of the perturbation flow by the background velocity $\sim \alpha A \cos XG$. However, the perturbation plotted in figure 5(*d*) shows that advection cannot dominate everywhere; the temperature gradient changes by an $O(1)$ amount through regions centred on $X = 2n\pi$ for integer n, which suggests the presence of boundary layers in which horizontal diffusion enters the leading-order balance.

We first observe that the linearized governing equations (3.2) exhibit a number of symmetries. Suppose that, for a given eigenvalue $\sigma(A, \alpha)$, we have solutions $[F(X), G(X)]$. It is clear from the form of (3.2) that $[-F(-X), G(-X)]$, $[F(2\pi + X), G(2\pi + X)]$, and $[-F(2\pi - X), G(2\pi - X)]$ are all also solutions, as are any

linear combinations of these. Thus, we are free to construct solutions with any given reflectional symmetry around $X = 0$ and $X = \pm\pi$. Motivated by the symmetries of the most unstable mode shown in figure 5, we consider a solution $[F, G]$ in which G is even under reflection about $X = 0$ and odd under reflection about $X = \pm\pi$, and F is odd under reflection about $X = 0$ and even under reflection about $X = \pm\pi$. Such a solution is periodic with period 4π.

As discussed above, we anticipate boundary-layer regions located near $X = 2n\pi$, for integer n, in which horizontal diffusion (G'') enters the leading-order balance in (3.2*b*). We therefore look for an asymptotic solution over the range $0 \leqslant X \leqslant 2\pi$, which has the symmetries of $[F, G]$ discussed above, with an inner region near $X = 0$ where diffusion is important, and an outer region away from $X = 0$ where the advection terms dominate.

In order to motivate the asymptotic scalings, we also recall the measured scalings from the full Floquet analysis of § 3 for the growth rate $\mathrm{Re}\{\sigma\} \sim A^{4/9}$, the phase speed $c_M = -\mathrm{Im}\{\sigma\}/\alpha_M = A$, and the vertical wavenumber $\alpha_M \sim A^{-1/9}$ (see (3.8) and (3.9)).

4.1. *Asymptotic expansion*

We consider the limit of large amplitude A and of small vertical wavenumber α, such that $\alpha A \gg 1$ and $\alpha \ll 1$, and we try

$$\sigma = -\mathrm{i}\sigma_0 \alpha A + \sigma^*, \tag{4.1}$$

where $|\sigma^*| \ll \alpha A$, and σ_0 is an $O(1)$ constant to be determined. The perturbation equations (3.2) can be rewritten as

$$F'' + G' = \alpha^2 F, \quad \mathrm{i}\alpha A\,(\cos X - \sigma_0)\,G - \mathrm{i}\alpha A \sin X F + \sigma^* G + F' = G'' - \alpha^2 G. \tag{4.2a,b}$$

The boundary conditions come from the symmetries of the solution as discussed above, and are given by

$$F(0) = G'(0) = G(\pi) = F'(\pi) = 0. \tag{4.3}$$

Based on the limits $\alpha A \gg 1$, $\alpha \ll 1$, the leading-order behaviour of (4.2) away from $X = 0$ is given by

$$F' + G = c_0, \quad (\cos X - \sigma_0)\,G - \sin X F = 0, \tag{4.4a,b}$$

where c_0 is a constant of integration that comes from the first integral of (4.2*a*). Equation (4.4) has solutions

$$F = (\cos X - \sigma_0)\left(1 + c_0 \int \frac{\mathrm{d}X}{\cos X - \sigma_0}\right), \quad G = \sin X \left(1 + c_0 \int \frac{\mathrm{d}X}{\cos X - \sigma_0}\right), \tag{4.5a,b}$$

where, without loss of generality, the arbitrary amplitude of the perturbations has been scaled to unity. Based on the form of the numerical solutions in figure 5, we assume that there are no leading-order discontinuities in F at $X = 0$ or in G at $X = \pi$. The boundary conditions (4.3) thus imply that $\sigma_0 = 1$ and that $c_0 = 0$, such that the leading-order outer solutions are given by

$$F = \cos X - 1, \quad G = \sin X. \tag{4.6a,b}$$

The leading-order phase speed $c = -\mathrm{Im}\{\sigma\}/\alpha = \sigma_0 A$ is given by $c = A$, as we found numerically in (3.8*b*)

Since $\sigma_0 = 1$, the coefficients $\cos X - \sigma_0$ and $\sin X$ of the $O(\alpha A)$ terms in (4.2*b*) both vanish as $X \to 0$, which suggests an inner boundary-layer region there, as indicated by the numerical solutions. We look for a balance in (4.2*b*) between the advection terms, horizontal diffusion G'' and growth $\sigma^* G$. This balance gives $\alpha A X^2 G \sim \alpha A X F \sim \sigma^* G \sim G/X^2$. From (4.6*b*), we also have that $G \sim X$ as $X \to 0$. Based on these balances, we define the following inner variables:

$$\xi = (\alpha A)^{1/4} X; \quad s = (\alpha A)^{-1/2} \sigma^*; \quad g(\xi) = (\alpha A)^{1/4} G(X); \quad f(\xi) = (\alpha A)^{1/2} F(X). \tag{4.7a,b,c,d}$$

Rewritten in terms of the inner variables, the governing equations (4.2) become

$$f'' + g' = \alpha^2 (\alpha A)^{-1/2} f, \quad g'' - \left(s - \frac{\mathrm{i}\xi^2}{2} \right) g + \mathrm{i}\xi f = (\alpha A)^{-1/2} \left(f' + \alpha^2 g \right). \tag{4.8a,b}$$

At leading order,

$$f' + g = \gamma_0, \quad g'' - \left(s - \frac{\mathrm{i}\xi^2}{2} \right) g + \mathrm{i}\xi f = 0. \tag{4.9a,b}$$

The constant of integration γ_0 in (4.9*a*) is determined by matching with the outer region: by integrating (4.2*a*) and substituting from (4.6*a*), we obtain to leading order

$$F' + G = \alpha^2 \int_\pi^X (\cos X - 1)\, \mathrm{d}X = \alpha^2 (\sin X - X + \pi), \tag{4.10}$$

where the lower limit of the integral has been determined from the boundary conditions (4.3*c,d*). The right-hand side of (4.10) is given by $\alpha^2 \pi$ to leading order as $X \to 0$, which, together with the inner scalings (4.7*c,d*), determines the constant of integration in (4.9*a*) as

$$\gamma_0 = \alpha^2 (\alpha A)^{1/4} \pi = \left(\alpha A^{1/9} \right)^{9/4} \pi. \tag{4.11}$$

The boundary conditions for (4.9) are given by the two symmetry conditions (4.3*a,b*) $f(0) = g'(0) = 0$ and a matching condition that $g \to \xi$ as $\xi \to \infty$. In appendix A, we consider the generic behaviour of the solutions of (4.9), and find that the matching condition constitutes two constraints on the differential equation; we therefore have four conditions on a third-order system, which is sufficient to determine the unknown eigenvalue s. We solve (4.9) numerically, and determine s as a function of the rescaled vertical wavenumber

$$\alpha^* \equiv \alpha A^{1/9}, \tag{4.12}$$

(cf. (4.11)). The leading-order growth rate is then given by $\mathrm{Re}\{\sigma^*\} = (\alpha A)^{1/2}\, \mathrm{Re}\{s(\alpha^*)\}$ from (4.7*b*), or alternatively

$$\mathrm{Re}\{\sigma^*\} = A^{4/9} \mathrm{Re}\{S(\alpha^*)\} \quad \text{where } S(\alpha^*) = \alpha^{*1/2} s(\alpha^*). \tag{4.13}$$

Numerical solutions for the leading-order scaled growth rate $\mathrm{Re}\{S(\alpha^*)\}$ are shown in figure 6(*a*). The eigenvalue with the maximum growth rate is given by $S = 0.2308 - 0.182\mathrm{i}$ and occurs at $\alpha^* = 0.332$, such that $\mathrm{Re}\{\sigma^*\} = 0.2308 A^{4/9}$ at $\alpha = 0.332 A^{-1/9}$. These values agree extremely well with the measurements presented in Figures 3(*a*) and 4(*a*) for the maximum growth rate $\mathrm{Re}\{\sigma_M\}$ and the corresponding vertical wavenumber α_M, respectively. Since the imaginary part of S is negative, the second-order correction to the phase speed is positive, and is given

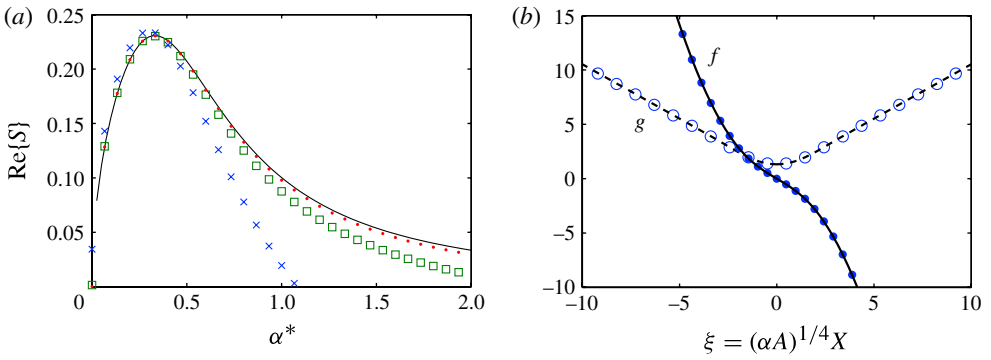

FIGURE 6. (Colour online) Asymptotic solutions ($A \gg 1$) and full numerical solutions of the eigenvalue problem (3.6). (*a*) The leading-order scaled growth rate $\mathrm{Re}\{S\} = \alpha^{*1/2}\mathrm{Re}\{s\} = A^{-4/9}\mathrm{Re}\{\sigma^*\}$ against the scaled vertical wavenumber $\alpha^* = \alpha A^{1/9}$: the asymptotic solution (line), and the full numerical solutions for $A = 2^{10}$ (crosses), $A = 2^{20}$ (squares) and $A = 2^{30}$ (dots). (*b*) The solution $[f, g] = [(\alpha A)^{1/2}F, (\alpha A)^{1/4}G]$ (solid and dashed lines, respectively) of (4.9), together with full solutions of (3.6) for $A = 2^{30}$ (solid and hollow circles, respectively).

by $-\mathrm{Im}\{\sigma^*\}/\alpha = 0.55A^{5/9}$. The dependence of $\mathrm{Re}\{S\}$ on the wavenumber α^* (figure 6*a*) shows very good agreement between the asymptotic analysis and the full solutions of the Floquet analysis for large A, as do the eigenfunctions $[f, g]$ of (4.9), which give the leading-order behaviour of $[F, G]$ near $X = 0$ (figure 6*b*).

The leading-order growth rate $\mathrm{Re}\{S(\alpha^*)\}$ increases for small α^* and decreases for large α^* (figure 6*a*). In appendix B, in order to understand this behaviour, we analyse the leading-order equations for the inner region (4.9) in the asymptotic limits $\alpha^* \ll 1$ and $\alpha^* \gg 1$. The physical basis for the decay in the growth rate at small and large α^* is discussed below.

4.2. *Physical mechanism of instability for* $A \gg 1$

It has proved difficult to unravel the precise details of the physical mechanism of instability, largely owing to the fact that the growth rate depends on a subtle second-order interaction between boundary-layer regions and the main flow. However, based on the form of the asymptotic equations, we can make various observations about the relevant physical components that control the propagation and growth of perturbations.

The leading-order evolution of the most unstable perturbation for $A \gg 1$ is neutral propagation at speed $c = \pm A$, which is the maximum speed of the background flow. The neutral propagation is the result of a leading-order advective balance between two processes: horizontal advection of the background temperature field Θ_0 by the perturbation velocity $\widetilde{U}$, and vertical advection of the perturbation temperature field $\widetilde{\Theta}$ by the background velocity W_0. We illustrate this balance by working in a frame of reference moving with the perturbation, as sketched in figure 7. We consider an upwards propagating perturbation ($c = +A$), but the discussion equally applies to downwards propagating perturbations. Since the vertical wavenumber α^* is small, Darcy's law implies that the perturbation temperature $\widetilde{\Theta}$ and vertical velocity $\widetilde{W}$ are proportional. By mass conservation, the horizontal velocity $\widetilde{U}$ is strongest where the vertical variation of $\widetilde{W}$ is largest, which occurs where $\widetilde{W}$ vanishes. The perturbation flow therefore takes the form of tall thin circulating cells. Horizontal advection of Θ_0 by $\widetilde{U}$ leads to an induced temperature perturbation (shown dashed on the right-hand

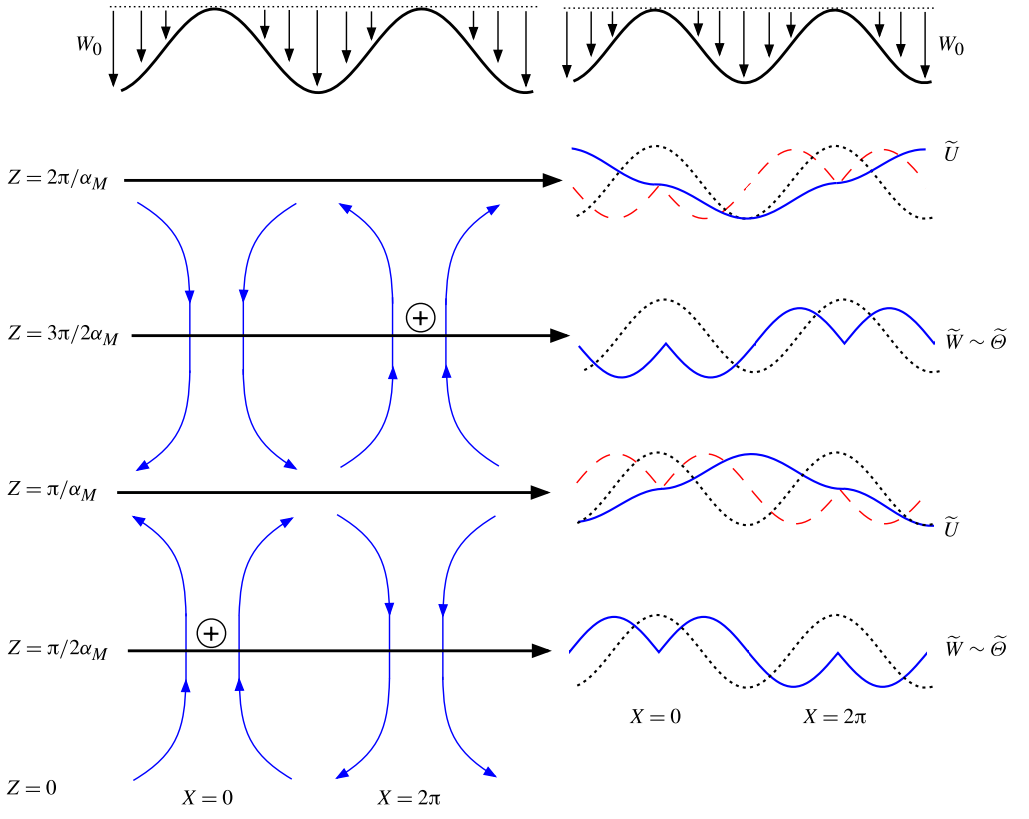

FIGURE 7. (Colour online) A schematic of the instability for $A \gg 1$, in a frame of reference moving with the perturbation. The background vertical velocity $W_0 = A\cos X - A$ in this frame is shown at the top. The left-hand side shows streamlines of the perturbation flow; the perturbation temperature $\widetilde{\Theta}$ is proportional to the vertical velocity $\widetilde{W}$, and locations at which pulses form on the background columns as a result of the instability are marked with a $\oplus$. The right-hand side shows horizontal profiles (all scaled to unit amplitude) along the lines of constant z as marked. Each plot shows the background temperature field Θ_0 (dotted), together with one of the perturbation velocities (solid) as labelled on the right; in each plot, the velocity not shown is zero. The plots at $Z = \pi/\alpha_M$ and $Z = 2\pi/\alpha_M$ also show the induced temperature perturbations (dashed) that result from horizontal advection of the background field Θ_0 by $\widetilde{U}$. The neutral propagation of the perturbation is sustained by downwards advection of the induced temperature perturbation by the background velocity W_0.

side of figure 7) that is vertically out of phase with the original temperature perturbation. Downwards vertical advection of the induced temperature perturbation by the background flow W_0 (in this propagating frame) balances the horizontal advection in such a way that the original perturbation is sustained.

The leading-order advective balance gives a neutrally propagating mode. Growth occurs because of horizontal diffusion in the thin boundary-layer regions centred on the lines $X = 2n\pi$, across which the temperature gradient changes significantly. The importance of diffusion can be seen by an examination of (4.9*b*), which shows that the two advective processes described above are balanced by diffusion (g'') and growth (sg) in these boundary-layer regions. Indeed, (4.9*b*) also shows that the advective processes, which have imaginary coefficients, and diffusion, which has a real

coefficient, are vertically out of phase, so that we might expect the rescaled eigenvalue s to have both a non-zero imaginary part, which gives a correction to the phase speed, and a non-zero real part, which gives growth.

The strength of diffusion, which must determine the growth rate, depends on the rescaled vertical wavenumber α^*. We found in § 4.1 that the growth rate decreases at both large and small α^* (figure 6*a*). For $\alpha^* \ll 1$, the perturbation cells are very long and, by continuity, the horizontal velocity is weak. The boundary-layer regions, which have a width that is set by the strength of the horizontal advection, are therefore wider (as in (4.7*a*)), so the diffusive flux is weaker, and the growth rate decreases. Conversely, for $\alpha^* \gg 1$, the horizontal velocity is strong. In this limit, the perturbation in the boundary-layer regions takes a different form: the temperature is smoothed out by strong horizontal advection, and the leading-order advective balance no longer gives discontinuities in the temperature gradient (see appendix B). Owing to this smoothed temperature profile, diffusion only enters the balance at higher-order, and so both the diffusive flux and the growth rate decrease. We therefore find that there is a balance between diffusion being too weak for $\alpha^* \ll 1$ and horizontal velocity being too strong for $\alpha^* \gg 1$, which gives rise to an optimal wavenumber $\alpha^* = 0.332$ at which the growth rate is maximum.

Interestingly, the instability process discussed above is independent of the background linear temperature gradient. Indeed, the analysis of § 4.1 shows that the term describing advection of the background temperature gradient (F') does not enter the asymptotic equations. This contrasts with the control of the instability for small A by the background temperature gradient.

Another interesting implication of the above discussion is that thermal diffusion provides a destabilizing mechanism for the flow. In appendix C, we examine a related system of columnar-exchange flow of two fluids of different densities in the absence of diffusion, and we find that the flow is always neutrally stable. This observation supports the idea that diffusion is required for the growth of perturbations. There is some parallel between the role of thermal diffusion here and the role of viscosity in the stability of plane Poiseuille flow (e.g. Drazin 2002), where the flow is linearly unstable for sufficiently large Reynolds numbers, but is linearly stable in the inviscid limit.

5. Evolution of the instability in the nonlinear regime

In order to explore the development of the instability beyond the linear regime, we examined heat-exchanger flow using high-resolution direct numerical simulations. We set the temperature $\Theta = \Theta_0 + \widetilde{\Theta}$ to be the steady heat-exchanger solution $\Theta_0 = A\cos X - Z$, as in (2.8*a*), plus an initially small perturbation $\widetilde{\Theta}(X, Z, \tau)$, and then solved the nonlinear governing equations (2.7) for the evolution of $\widetilde{\Theta}$ numerically. In order to clearly observe the nonlinear evolution of the instability, we used doubly periodic boundary conditions for $\widetilde{\Theta}$ and for the corresponding streamfunction $\widetilde{\Psi}$ (given by (2.7*a*)). We used a vertical period of $2\pi/\alpha_M \approx 18.9A^{1/9}$, which is the height of the most unstable mode calculated in § 3. The initial value of $\widetilde{\Theta}$ was proportional to the most unstable mode.

Snapshots of the temperature field Θ at different times for $A = 2^8 = 256$ and horizontal period $L = 8\pi$ are shown in figure 8(*a–d*), together with the corresponding magnitude of the perturbation over time (figure 8*e*) and dominant wavenumber of the flow (figure 8*f*). The linear growth of the instability leads to the formation of pulses (figure 8*a*) which move with the background flow. Once the pulses have

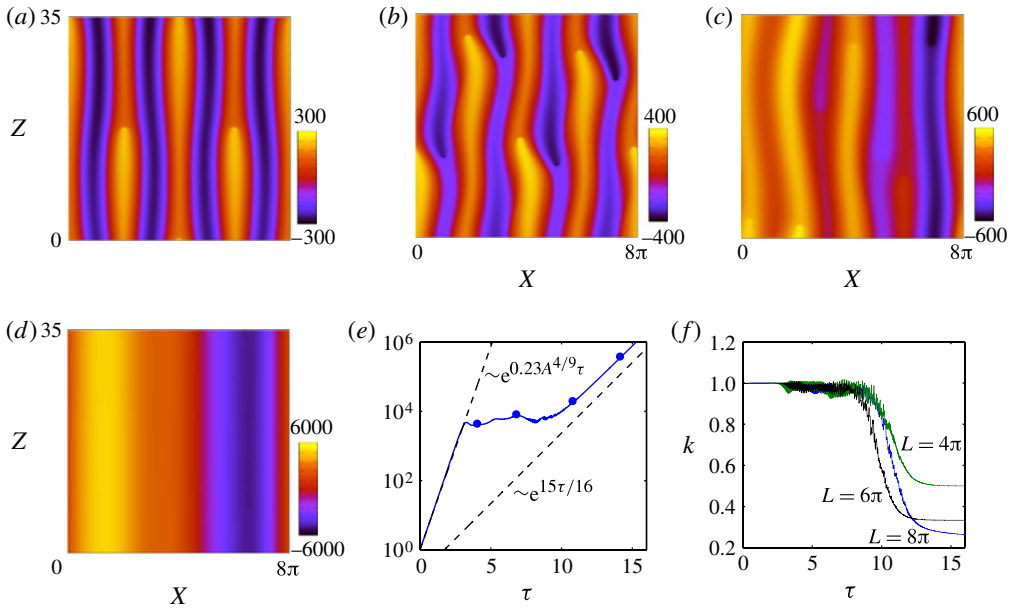

FIGURE 8. (Colour online) Nonlinear dependence of the instability for $A = 2^8$ and horizontal period $L = 8\pi$. Snapshots of the temperature field $\Theta(X, Z, \tau)$ at times: (*a*) $\tau = 4$, the growth of pulses on the background flow that result from linear instability; (*b*) $\tau = 7$ and (*c*) $\tau = 11$, the secondary instability; and (*d*) $\tau = 14$, the growing heat-exchanger flow with a quarter of the original wavenumber (5.1). (*e*) The magnitude of the perturbation over time, as measured by the L2 norm and scaled by the initial magnitude; dots correspond to the pictures in the previous panels. The asymptotic growth of the most unstable mode (from (3.8*a*)) and the growth of the unsteady exchange flow equation (5.1) are also shown, for comparison. (*f*) The dominant wavenumber k of the flow (measured by a Fourier transform of the temperature field at $Z = 0.5$), for simulations with different horizontal periods L as marked; in each case, the wavenumber decreases towards the fundamental mode $2\pi/L$.

reached a certain size, the amplitude stops growing, and the flow becomes unstable to a secondary instability, which breaks the symmetry of the solution and results in less regular motion (figure 8*b,c*). The system gradually re-organizes into columnar flow with a quarter of the wavenumber of the original flow (figure 8*d*), but the same background temperature gradient, which remains imposed by the representation $\Theta = \Theta_0 + \widetilde{\Theta}$.

However, the wavenumber and background gradient of a steady heat-exchanger flow are linked by (2.5*a*); hence, if the wavenumber decreases and the gradient is fixed, the flow can no longer be a steady solution of the governing equations. Instead, we find that the amplitude of the flow grows exponentially (figure 8*e*). It is straightforward to show that the governing equations permit unsteady columnar flow with a fixed background temperature gradient for any wavenumber κ; this generalized time-dependent columnar flow is given by

$$\Theta = A\mathrm{e}^{(1-\kappa^2)\tau}\cos\kappa X - Z, \quad W = A\mathrm{e}^{(1-\kappa^2)\tau}\cos\kappa X, \tag{5.1a,b}$$

for any amplitude A. The steady solution $\kappa = 1$ (2.8) can be thought of as the marginally stable solution: if $\kappa > 1$, horizontal diffusion dominates and the amplitude decays; if $\kappa < 1$, advection dominates and the amplitude grows. In the results of

figure 8, the system ultimately adopts a wavenumber $\kappa = 1/4$, and the magnitude of the flow grows like $\mathrm{e}^{15\tau/16}$ (figure 8*e*). We note that the continued exponential growth at late times only arises because it can feed off the fixed background temperature gradient that is imposed in an effectively infinite domain.

The main conclusion from this calculation is that the nonlinear evolution of the instability leads to a reduction of the wavenumber of the flow. We have also carried out simulations in domains with different horizontal periods L; in each case the flow coarsened due to a secondary instability, leaving one upwelling and one downwelling column in the domain (figure 8*f*).

6. Implications for convection in a porous medium

In this section, we return to the linear-stability analysis of § 3 and consider the implications of this analysis for columnar flow in a vertically confined domain. Specifically, we investigate whether stability might provide the mechanism that controls the horizontal scale of the columnar flow in the interior of a Rayleigh–Darcy cell at high Ra.

6.1. *The wavenumber of columnar flow in a Rayleigh–Darcy cell at high Ra*

Flow in a Rayleigh–Darcy cell for $Ra \gtrsim 1300$ is dominated in the interior by columnar flow. This nearly steady interior flow is fed from the upper and lower boundaries of the cell by vigorous mixing and merging of short-wavelength proto-plumes (see figure 1*a*). Numerical measurements from a cell of height $H = 1$ over the range $1300 \leqslant Ra \leqslant 4 \times 10^4$ (Hewitt *et al.* 2012) suggest that the columnar flow in the interior of the cell is increasingly well described by the steady heat-exchanger solution in (2.5) as $Ra \to \infty$. Measurements of the dominant wavenumber k over the same range were approximated by $k \approx 0.47Ra^{0.4}$, although there are significant fluctuations in the data, and there is some suggestion of a slightly weaker exponent at very large Ra.

It is important to note that there are some significant differences between the columnar flow in a Rayleigh–Darcy cell at high Ra and the steady unconfined heat-exchanger flow that has been the subject of this paper so far. Most notably, the cell has a finite height and the flow in the interior is fed by time-dependent proto-plumes at the upper and lower boundaries as discussed above, whereas the heat-exchanger flow (2.5) has an infinite height, and any disturbances propagate indefinitely. It is, nonetheless, interesting to try applying some of the results from the stability of unconfined heat-exchanger flow to the flow in a vertically confined domain, and to compare the resultant scalings of this simple analysis with numerical measurements of the dominant wavenumber k.

In ideal heat-exchanger flow, the amplitude of the temperature and vertical velocity are equal, as in (2.5). In a Rayleigh–Darcy cell, numerical measurements (Hewitt *et al.* 2012) show that the amplitude of the temperature $\hat{T}$ and vertical velocity $\hat{w}$ tend to approximately the same constant value, $\hat{T}, \hat{w} \to 0.117$, as $Ra \to \infty$. However, for finite Ra, $\hat{T}$ is somewhat larger than $\hat{w}$ (figure 9). There is, therefore, an ambiguity about which measurement to use. Since $\hat{w}$ varies less than $\hat{T}$ over the measured range of Ra, we choose to set $\widehat{A} = \hat{w}$ for the following analysis (although, in fact, we find very little difference if $\hat{T}$ is used instead).

In a vertically confined domain, we hypothesize that a perturbation to the steady columnar flow will destabilize the flow if the time scale for growth of the perturbation is shorter than the time scale for the perturbation to advect from one boundary to the other. We assume that the regions of proto-plumes at the upper and lower

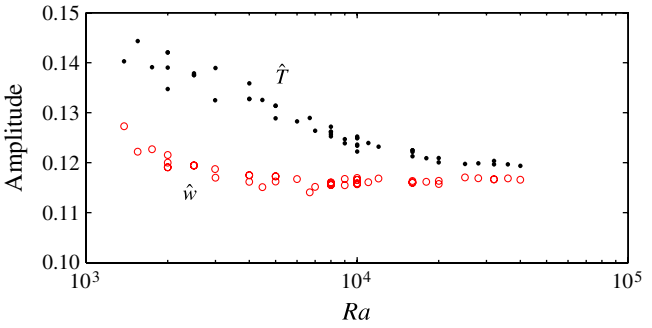

FIGURE 9. (Colour online) Measurements of the amplitude of the temperature $\hat{T}$ (dots) and vertical velocity $\hat{w}$ (circles) of the columnar flow in the interior of a Rayleigh–Darcy cell (adapted from figure 3 of Hewitt *et al.* (2012)). The amplitudes appear to tend to approximately the same constant value, $\hat{T}, \hat{w} \to 0.117$, as $Ra \to \infty$. (This result is directly equivalent to the asymptotic 'classical' linear scaling of the Nusselt number with Ra, as observed by Hewitt *et al.* (2012).) For comparison with the linear-stability analysis, we choose $\widehat{A} = \hat{w}$.

boundaries provide perturbations to the columnar flow on a range of scales. Since the height of the Rayleigh–Darcy cell in rescaled co-ordinates (§ 2.2) is $H = k$, the time scale for advection of the most unstable perturbation across the domain for $A \gg 1$ is $H/c_M = k/A$ (from (3.8*b*)), and the time scale for growth of the most unstable perturbation is $1/\mathrm{Re}\{\sigma_M\} = 1/(0.231A^{4/9})$ (from (3.8*a*)). A comparison of these time scales, which is the hypothesized condition for instability, gives

$$\frac{k}{A} \gtrsim \frac{1}{0.231A^{4/9}} \quad \text{for } A \gg 1, \tag{6.1}$$

which reduces to

$$k \gtrsim 2.6\left(\hat{w}Ra\right)^{5/14} \gtrsim 1.2Ra^{5/14} \quad \text{for } Ra \gg 1, \tag{6.2}$$

on using $A = \widehat{A}Ra/k = \hat{w}Ra/k$ and the observation that $\hat{w} \to 0.117$ as $Ra \to \infty$. We note that, since (6.2) is simply obtained by a comparison of time scales, we would not expect the numerical prefactor in (6.2) to be accurate, beyond giving a rough estimate of the order of magnitude.

For $A \lesssim O(10^4)$, both the growth rate and the phase speed of the most unstable mode are found numerically to be slightly larger than the asymptotic scalings (3.8) (see the inset to figure 3). In addition, for $Ra \lesssim O(10^4)$, the amplitude $\hat{w}$ is slightly larger than its asymptotic value (see figure 9). We found simple empirical fits $\mathrm{Re}\{\sigma_M\} \approx 0.231A^{4/9} + 0.34A^{-0.2}$ and $c_M \approx A + 0.55A^{0.55}$ to the numerical data for $A \gtrsim 17.2$, and $\hat{w} \approx 0.117 + 2900Ra^{-1.8}$ to the amplitude for $Ra \geqslant 1300$. By using these fits in the balance of time scales $k/c_M \sim 1/\mathrm{Re}\{\sigma_M\}$, as above, with $A = \hat{w}Ra/k$, we obtain a correction for finite Ra and A to the asymptotic stability estimate (6.2). This approximate correction $k(Ra)$ is given implicitly by the equations

$$k = \frac{A + 0.55A^{0.55}}{0.231A^{4/9} + 0.34A^{-0.2}}; \quad kA = Ra\left(0.117 + 2900Ra^{-1.8}\right). \tag{6.3}$$

Figure 10(*a*) shows measurements of the time-averaged dominant wavenumber $k(Ra)$ from a Rayleigh–Darcy cell for $1300 < Ra \leqslant 4 \times 10^4$, together with the

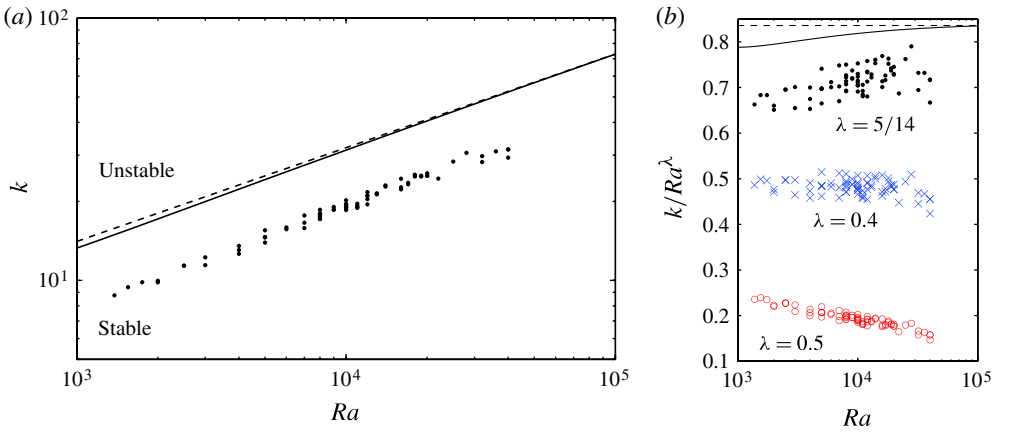

FIGURE 10. (Colour online) Measurements of the wavenumber k from a Rayleigh–Darcy cell of height $H = 1$ and aspect ratio either $L = 1$ or $L = 2$, taken from Hewitt *et al.* (2012): (*a*) the wavenumber $k(Ra)$ (dots) together with the asymptotic stability estimate (6.2) (dashed line) and the approximate correction to the asymptotic scaling for finite Ra and A from (6.3) (solid line); and (*b*) the scaled wavenumber k/Ra^{λ} for trial exponents $\lambda = 5/14$ (dots), $\lambda = 0.4$ (crosses) and $\lambda = 0.5$ (circles), together with the asymptotic stability estimate (6.2) (dashed line) and the correction from (6.3) (solid line), both scaled by $0.7Ra^{5/14}$. The measured data follows the trend of the correction (solid line) over this range of Ra.

asymptotic stability estimate (6.2) (dashed line), and the approximate correction to the asymptotic scaling, given by the solution of (6.3) (solid line). The measured data lies inside the stable region, and appears to give good agreement with the trend of the stability estimates.

In order to examine this agreement more closely, we can rescale the wavenumber and the stability estimates by different trial powers of Ra (figure 10*b*). As a preliminary observation, we can see from this rescaling that the measured data exhibits a distinctly weaker scaling than $k \sim Ra^{1/2}$, which was identified as the 'minimal flow unit' for steady convection (Corson 2011). Instead, it appears that the data is fairly well described by the scaling $k \sim Ra^{0.4}$ over this range of Ra, which is slightly stronger than the asymptotic stability estimate $k \sim Ra^{5/14}$. However, it is also evident that the estimate corrected for finite Ra and A (solid line) differs appreciably from the asymptotic estimate (dashed line) over this range of Ra, and that the measured data follows the trend of the correction. (The parameter A for the data shown lies in the range $25 \lesssim A \lesssim 150$.) In particular, the data appears to show a slight trend towards a lower exponent at the highest values of Ra, in agreement with the prediction of the stability estimate.

The measured data does, therefore, appear to be consistent with the theoretical stability estimate. Given the very different boundary conditions between the Rayleigh–Darcy cell and the unconfined heat-exchanger flow, this qualitative agreement is notable. Figure 10(*b*) suggests that the Rayleigh number for the measured data is still too low to observe the hypothesized asymptotic scaling $k \sim Ra^{5/14}$; numerical measurements of k at higher values of Ra would be needed to confirm this suggestion.

6.2. *The onset of the high-Ra regime in a Rayleigh–Darcy cell*

Working on the hypothesis that stability controls the horizontal scale of the interior flow in a Rayleigh–Darcy cell, it is natural to consider what happens as Ra decreases or, equivalently, as the rescaled amplitude of the flow A decreases. In § 3.2, we found that the nature of the dominant instability in an unbounded domain changes completely when $A \lesssim 17.2$. A similar dramatic change is observed in the dynamics of the Rayleigh–Darcy cell as Ra decreases below $Ra \approx 1300$ (Graham & Steen 1994; Otero *et al.* 2004), from columnar-exchange flow in the interior for $Ra \gtrsim 1300$ to large-scale convective rolls for $Ra \lesssim 1300$.

Measurements of k and $\widehat{A} = \hat{w}$ (Hewitt *et al.* 2012) at $Ra = 1380$, which is just above the transition point, give a value of $A \approx 14.5$ (alternatively, using $\widehat{A} = \hat{T}$ gives $A \approx 15.6$), which is remarkably close to the bifurcation value $A \approx 17.2$ in the linear-stability problem. In fact, since the most unstable mode of the unbounded flow for $A < 17.2$ has zero wavenumber in both directions, which is not physically achievable in a finite domain, we would expect the Rayleigh–Darcy cell to have a slightly lower bifurcation value of A. The rough agreement demonstrated here provides an intriguing direction for further investigation, and again suggests that stability criteria may play an important role in the dynamical structure of the Rayleigh–Darcy cell.

7. Conclusions

We have examined the stability of columnar convection in a porous medium. The flow is characterized by dimensionless horizontal wavenumber k, amplitude $\widehat{A}$ and background temperature gradient $-k^2/Ra$. The stability of the flow in an unbounded domain is then a function of the parameter $A = \widehat{A}Ra/k$ alone.

We used a Floquet analysis to determine the eigenvalues σ of the linear-stability problem (3.2) numerically. Somewhat surprisingly, the marginal-stability curve $\mathrm{Re}\{\sigma\} = 0$ is independent of A and thus given by the usual criterion $\beta = \beta^2 + \alpha^2$ for stability of a linear temperature field, where β and α are the horizontal and vertical wavenumbers, respectively. For small A, the most unstable mode is given by $\alpha = \beta = 0$, and has growth rate $\mathrm{Re}\{\sigma\} = 1$; this mode is an instability of the background linear temperature gradient and is independent of the columnar flow. However, at $A \approx 17.2$, a different mode becomes the most unstable. This mode has double the horizontal period of the background flow ($\beta = 1/2$), takes the form of vertically propagating pulses on the background columns and has a growth rate that increases with A. Asymptotically, the vertical wavenumber of the most unstable mode is given by $\alpha = 0.332A^{-1/9}$, the growth rate by $\mathrm{Re}\{\sigma\} = 0.2308A^{4/9}$ and the vertical phase speed by $|c| = A$. The sign of c changes if the perturbation is shifted horizontally by π (a quarter period).

For $A \gg 1$, advective processes dominate the flow across almost all of the domain: horizontal advection of the background temperature by the perturbation flow balances vertical advection of the perturbation temperature by the background flow. In the absence of any diffusion, this advective balance would simply give a neutrally stable propagating mode. However, the temperature gradient changes significantly across thin boundary-layer regions that are centred on the maxima (for upwelling perturbations) or minima (for downwelling perturbations) of the background flow. Horizontal diffusion in these boundary-layer regions provides a mechanism for growth, as discussed in § 4.2. Interestingly, the instability is independent of the background

vertical temperature gradient in the limit $A \gg 1$, and is driven entirely by the columnar flow.

Numerical simulations of the nonlinear evolution of the instability for $A \gtrsim 17.2$ in a periodic domain show that perturbations initially grows in accordance with linear theory, before the flow undergoes a secondary instability. After a period of reorganization, the system evolves into a new columnar flow with a smaller wavenumber than the original flow.

Persistent vertical columnar structures have also been observed in three-dimensional porous convection (e.g. Pau *et al.* 2010; Fu *et al.* 2013), and it seems likely that many of the ideas discussed in this paper could be extended to three dimensions. However, while it is straightforward to write down three-dimensional heat-exchanger base flows, the linear-stability analysis of such flows is much more complicated than in two dimensions (primarily owing to the double expansion in the Floquet analysis). Such analysis is left for future work, along with detailed investigation of the interior horizontal planform of statistically steady three-dimensional porous convection.

This work was motivated by the hitherto unexplained mechanism that controls the horizontal wavenumber of the columnar flow in the interior of a two-dimensional Rayleigh–Darcy cell at high Ra. Numerical measurements of this flow suggest that it is increasingly well described by the steady heat-exchanger solution as $Ra \to \infty$. By a comparison of the time scales for growth and propagation of the most unstable mode, we derived an asymptotic stability estimate $k \sim (\widehat{A}Ra)^{5/14}$ for the wavenumber k of vertically confined heat-exchanger flow. In a Rayleigh–Darcy cell, the amplitude $\widehat{A}$ is given by the amplitude of the temperature $\hat{T}$ or the vertical velocity $\hat{w}$, which numerical measurements suggest are asymptotically equal and independent of Ra. The estimated stability boundary thus reduces to $k \sim Ra^{5/14}$ as $Ra \to \infty$. For $Ra < O(10^5)$, the stability boundary has a slightly stronger dependence on Ra than this asymptotic scaling. Although numerical measurements in a Rayleigh–Darcy cell at higher Ra would be required to verify the asymptotic scaling $k \sim Ra^{5/14}$, the stability boundary gives good agreement with the previously unexplained trend of numerical measurements of $k(Ra)$ over the range $1300 < Ra \leqslant 4 \times 10^4$.

The results of this paper, therefore, support the hypothesis that the stability of the interior columnar flow provides the mechanism that controls the wavenumber k in Rayleigh–Darcy convection. The vigorous large-wavenumber dynamics of proto-plume formation at the upper and lower boundaries force the system over a range of small scales, and the columnar flow adopts the smallest scale for which it can remain stable over the height of the domain, which is given by $k \sim Ra^{5/14}$ as $Ra \to \infty$. Any smaller-scale of columnar flow would be unstable, and the resulting instability would lead to a coarsening of the flow.

Appendix A. Generic behaviour of solutions of (4.9)

Equation (4.9) can be rewritten as a single differential equation for f by substituting $g = \gamma_0 - f'$ into (4.9*b*) to obtain

$$f''' + \left(\frac{\mathrm{i}\xi^2}{2} - s\right) f' - \mathrm{i}\xi f = \gamma_0 \left(\frac{\mathrm{i}\xi^2}{2} - s\right). \tag{A 1}$$

We seek solutions that satisfy $f(0) = f''(0) = 0$ and the matching condition $f \to -\xi^2/2$ (equivalently $g \to \xi$) as $\xi \to \infty$. In order to determine the unknown eigenvalue s, we require four boundary conditions for the third-order system (A 1). It is not clear,

per se, whether the matching condition constitutes one or two constraints; this depends on the generic behaviour of the solutions as $\xi \to \infty$.

A WKB approximation to (A 1) in the limit $\xi \to \infty$ gives leading-order solutions of the form

$$f \sim c\,\xi^2 - \gamma_0 \xi + d_\pm\, \xi^b \exp\left[\pm \frac{(1-\mathrm{i})}{4}\xi^2\right] + O(1) \quad \text{as } \xi \to \infty, \tag{A 2}$$

where b would be determined at the next order, and c and $d_\pm$ are constants. The matching condition $f \to -\xi^2/2$ requires both that $c = -1/2$ and that $d_+ = 0$. It therefore constitutes two constraints, and we have sufficient conditions to determine the eigenvalue s in (4.9).

Appendix B. Variation of the growth rate $\mathrm{Re}\{S\}$ for $\alpha^* \ll 1$ and $\alpha^* \gg 1$

In § 4.1, we determined the leading-order growth rate $\mathrm{Re}\{\sigma^*\} = A^{4/9}\mathrm{Re}\{S\}$ as a function of the rescaled vertical wavenumber α^*, and found that $\mathrm{Re}\{S(\alpha^*)\}$ increased for small α^* and decreased for large α^* (figure 6*a*). In this appendix, in order to understand this behaviour, we examine the limits $\alpha^* \ll 1$ and $\alpha^* \gg 1$. For clarity, we rewrite (4.9) and (4.13) here as

$$f' + g = \alpha^{*9/4}\pi, \quad g'' - \left(s - \frac{\mathrm{i}\xi^2}{2}\right) g + \mathrm{i}\xi f = 0, \quad S = \alpha^{*1/2} s. \tag{B 1a,b,c}$$

The boundary conditions are $f(0) = g'(0) = 0$ and $g \to \xi$ as $\xi \to \infty$.

In the limit $\alpha^* \ll 1$, (B 1*a*) becomes $f' = -g$ to leading order, while (B 1*b*) remains unchanged; the solution to these equations gives an eigenvalue $s = (1-\mathrm{i})/2$ that is independent of α^* to leading order. (The corresponding expression for the eigenfunction f can be found analytically in integral form, but the expression is not elucidating.) Hence,

$$\mathrm{Re}\{S\} = \tfrac{1}{2}\alpha^{*1/2} \quad \text{for } \alpha^* \ll 1. \tag{B 2}$$

In the limit $\alpha^* \gg 1$, the balance in (B 1*a*) requires that the eigenfunctions $[f, g]$ are $O(\alpha^{*9/4})$ to leading order. We write $g = \alpha^{*9/4} g_0 + g_1 + O(\alpha^{*-9/4})$ and $f = \alpha^{*9/4} f_0 + f_1 + O(\alpha^{*-9/4})$, and expand $s = s_0 + \alpha^{*-9/4} s_1 + O(\alpha^{*-9/2})$. The matching condition as $\xi \to \infty$ only applies at second order and is given by $g_1 \to \xi$; the first-order condition is instead given by $g_0 \to 2\pi$ (or, equivalently, $f_0 \to -\pi\xi$), which comes from the form of the solution as $\xi \to \infty$ given by (A 2*b*) in appendix A.

The solution of (B 1*a*,*b*) at leading order is simply given by $[f_0, g_0] = [-\pi\xi, 2\pi]$ and $s_0 = 0$; neither diffusion (g'') or growth (sg) enter the leading-order balance, which is instead simply between the advective terms. At second order, (B 1*a*,*b*) become

$$f_1' = -g_1, \quad g_1'' + \frac{\mathrm{i}\xi^2}{2} g_1 - 2\pi s_1 + \mathrm{i}\xi f_1 = 0, \tag{B 3a,b}$$

which can be solved numerically, together with boundary conditions $f_1(0) = g_1'(0) = 0$ and $g_1 \to \xi$ as $\xi \to \infty$, to give an eigenvalue $s_1 = 0.1164 - 0.048\mathrm{i}$. Thus,

$$\mathrm{Re}\{S\} = 0.1164\,\alpha^{*-7/4} \quad \text{for } \alpha^* \gg 1. \tag{B 4}$$

Figure 11 shows that the leading-order asymptotic predictions of $\mathrm{Re}\{S(\alpha^*)\}$ for small and large wavenumber from (B 2) and (B 4) give very good agreement with the full solution of figure 6(*a*). The physical basis for the decay in the growth rate at small and large α^* is discussed in § 4.2.

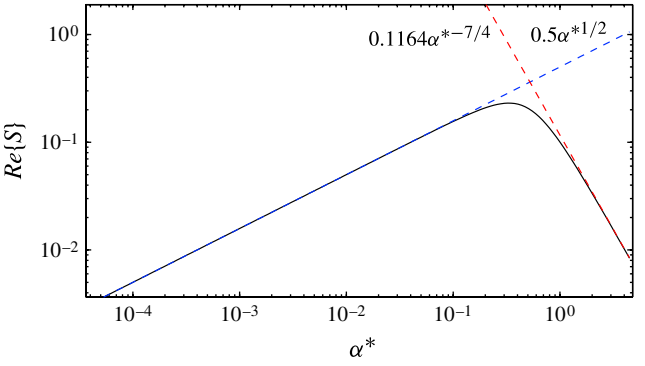

FIGURE 11. (Colour online) The leading-order growth rate Re$\{S\}$ (solid) as a function of the scaled vertical wavenumber α^*, together with the predictions from the asymptotic analysis for $\alpha^* \ll 1$ (B 2) and $\alpha^* \gg 1$ (B 4) (dashed).

Appendix C. Stability of piecewise uniform exchange flow in the absence of diffusion

In the main text of this paper, we examined the stability of density-driven heat-exchanger flow, in which vertical advection balanced horizontal diffusion between the interleaving columns. Motivated by the interesting observation in § 4.2 that diffusion acts as a destabilizing mechanism for the columnar flow, in this appendix we examine the related system of exchange flow of two distinct fluids of different densities in the limit of negligible diffusion. The fluids again flow in interleaving columns, as shown in figure 12.

The governing equations for the flow are incompressibility and Darcy's law (2.1). The system is horizontally periodic, and each period contains an upwelling column of unit width and uniform velocity w and a downwelling column of width λ^{-1} and velocity $-\lambda w$ by continuity (figure 12). The interface between the jth and $(j+1)$th columns is labelled by X_j. The density is piecewise uniform, and so the governing equations combine to give

$$\nabla^2 p = 0, \tag{C 1}$$

in each column.

We look for a pressure perturbation $\widetilde{p}_j$ in the jth column and a corresponding interfacial perturbation $\widetilde{X}_j$ of the form

$$\widetilde{p}_j = \pi_j(x)\exp(\sigma t + \mathrm{i}\alpha z)\,, \quad \widetilde{X}_j = \xi_j \exp(\sigma t + \mathrm{i}\alpha z)\,. \tag{C 2}$$

The horizontal variation π_j of the perturbed pressure is found by solving (C 1), which gives

$$\pi_j(x) = A_j \cosh\left[\alpha\left(x - X_j\right)\right] + B_j \sinh\left[\alpha\left(x - X_j\right)\right]. \tag{C 3}$$

The constants A_j, B_j and ξ_j are determined by continuity of pressure and a kinematic condition for each column at $X_j + \widetilde{X}_j$, which are linearized to give

$$\pi_j(X_j) = \pi_{j-1}(X_j), \tag{C 4a}$$

$$\left(\frac{\partial}{\partial t} + w_j\frac{\partial}{\partial z}\right)\widetilde{X}_j = -\left.\frac{\partial \widetilde{p}_j}{\partial z}\right|_{x=X_j}, \quad \left(\frac{\partial}{\partial t} + w_{j-1}\frac{\partial}{\partial z}\right)\widetilde{X}_j = -\left.\frac{\partial \widetilde{p}_{j-1}}{\partial z}\right|_{x=X_j}. \tag{C 4b}$$

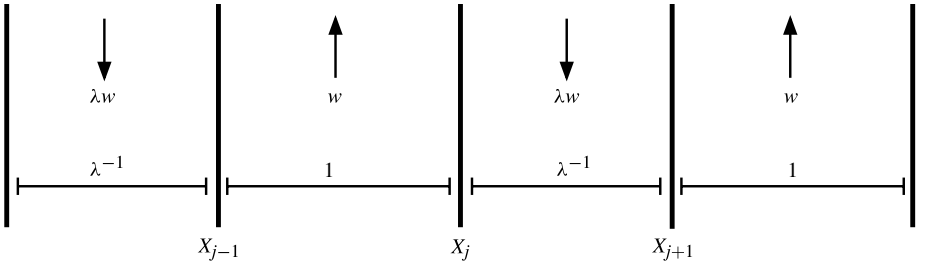

FIGURE 12. A schematic showing the interleaving flow of two distinct fluids of different densities, in columns with width ratio λ.

By substituting (C 2) into (C 4) and eliminating ξ_j, we obtain

$$A_{j+1} = A_j \cosh \alpha d_j + B_j \sinh \alpha d_j, \tag{C 5a}$$

$$B_{j+1} = \frac{\sigma + \mathrm{i}\alpha w_{j+1}}{\sigma + \mathrm{i}\alpha w_j} \left(A_j \sinh \alpha d_j + B_j \cosh \alpha d_j \right), \tag{C 5b}$$

where $[d_j, w_j]$ are the width and velocity of the jth column, given by $[1, w]$ for even j and $[\lambda^{-1}, -\lambda w]$ for odd j.

We consider perturbations that are periodic over $2N$ columns, for some integer N. Therefore, we equate the perturbations to the interface at X_{2N} with those at X_0. The application of (C 5) $2N$ times gives a dispersion relation for σ of the form

$$\det \left(\boldsymbol{M}^N - \boldsymbol{I} \right) = 0, \tag{C 6}$$

where $\boldsymbol{I}$ is the identity matrix. The matrix $\boldsymbol{M}$ is given by

$$\boldsymbol{M} = \begin{pmatrix} C_\lambda & S_\lambda \\ \Gamma S_\lambda & \Gamma C_\lambda \end{pmatrix} \begin{pmatrix} C_1 & S_1 \\ \Gamma^{-1} S_1 & \Gamma^{-1} C_1 \end{pmatrix}; \quad \Gamma = \frac{\sigma + \mathrm{i}\alpha w}{\sigma - \mathrm{i}\alpha\lambda w}, \tag{C 7a,b}$$

where $C_1 = \cosh \alpha$, $S_1 = \sinh \alpha$, $C_\lambda = \cosh(\alpha/\lambda)$ and $S_\lambda = \sinh(\alpha/\lambda)$.

Equation (C 6) has solutions if and only if $\boldsymbol{M}^N$ has eigenvalue 1, or equivalently $\boldsymbol{M}$ has an eigenvalue that is an Nth root of unity. Moreover, it is easily shown that the determinant of $\boldsymbol{M}$ is 1, and so the product of the eigenvalues of $\boldsymbol{M}$ is 1. Thus, equation (C 6) has solutions if and only if the eigenvalues of $\boldsymbol{M}$ are a conjugate pair of Nth roots of unity. We label these eigenvalues $\mu_\pm = a \pm \mathrm{i}b$, for some real a and b with $|a| \leqslant 1$, $|b| \leqslant 1$. Then (C 6) is equivalent to

$$\det \left(\boldsymbol{M} - \mu_\pm \boldsymbol{I} \right) = 0, \tag{C 8}$$

which can be reduced to

$$\left(1 + \Gamma^2 \right) S_1 S_\lambda + 2 \left(C_1 C_\lambda - a \right) \Gamma = 0, \tag{C 9}$$

Equation (C 9) is a quadratic for Γ, which has discriminant

$$\Delta = 4 \left[(C_1 - C_\lambda)^2 + 2(1 - a) C_\lambda C_1 + a^2 - 1 \right]. \tag{C 10}$$

Since $C_1 C_\lambda \geqslant 1$ and $|a| \leqslant 1$, equation (C 10) implies that $\Delta \geqslant (a - 1)^2 \geqslant 0$, and so solutions Γ of (C 9) must be real. This constraint, together with (C 7*b*), requires that σ is pure imaginary, which holds for any width ratio λ, velocity w, periodicity N or wavenumber α. Therefore, in the absence of diffusion, the columnar exchange

flow of two distinct fluids of different densities is neutrally stable to all wavelengths; perturbations are advected by the flow without growth or decay. This result is similar to the observation in § 4.2 that the leading-order advection balance for heat-exchanger flow gives neutral propagation and growth is only possible because of diffusion.

REFERENCES

AHLERS, G., GROSSMANN, S. & LOHSE, D. 2009 Heat transfer and large-scale dynamics in turbulent Rayleigh–Bénard convection. *Rev. Mod. Phys.* **81**, 503–537.

BACKHAUS, S., TURITSYN, K. & ECKE, R. E. 2011 Convective instability and mass transport of diffusion layers in a hele-shaw geometry. *Phys. Rev. Lett.* **106**, 104501.

BEAUMONT, D. N. 1981 The stability of spatially periodic flows. *J. Fluid Mech.* **108**, 461–474.

CHENG, P. 1978 Heat transfer in geothermal systems. *Adv. Heat Transfer* **14**, 1–105.

CORSON, L. T. 2011 Maximising the heat flux in steady unicellular porous media convection. In *Proceedings of the 2011 Geophysical Fluid Dynamics Summer Program*, pp. 389–412. Woods Hole Oceanographic Institution.

DRAZIN, P. G. 2002 *Introduction to Hydrodynamic Stability*. Cambridge University Press.

FOWLER, A. C. 1985 The formation of freckles in binary alloys. *IMA J. Appl. Maths* **35**, 159–174.

FU, X., CUETO-FELGUEROSO, L. & JUANES, R. 2013 Pattern formation and coarsening dynamics in three-dimensional convective mixing in porous media. *Phil. Trans. R. Soc.* A **371**, 20120355.

GRAHAM, M. D. & STEEN, P. H. 1994 Plume formation and resonant bifurcations in porous-media convection. *J. Fluid Mech.* **272**, 67–89.

HEWITT, D. R., NEUFELD, J. A. & LISTER, J. R. 2012 Ultimate regime of high Rayleigh number convection in a porous medium. *Phys. Rev. Lett.* **108**, 224503.

HEWITT, D. R., NEUFELD, J. A. & LISTER, J. R. 2013 Convective shutdown in a porous medium at high Rayleigh number. *J. Fluid Mech.* **719**, 551–586.

HIDALGO, J. J., FE, J., CUETO-FELGUEROSO, L. & JUANES, R. 2012 Scaling of convective mixing in porous media. *Phys. Rev. Lett.* **109**, 264503.

HOLYER, J. Y. 1981 On the collective instability of salt fingers. *J. Fluid Mech.* **110**, 195–207.

HOLYER, J. Y. 1984 The stability of long, steady, two-dimensional salt fingers. *J. Fluid Mech.* **147**, 169–185.

HUPPERT, H. E. & TURNER, J. S. 1981 Double-diffusive convection. *J. Fluid Mech.* **106**, 299–329.

JORDAN, D. W. & SMITH, P. 1999 *Nonlinear Ordinary Differential Equations*, 3rd edn. Oxford University Press.

LAPWOOD, E. R. 1948 Convection of a fluid in a porous medium. *Math. Proc. Camb. Phil. Soc.* **44**, 508–521.

METZ, B., DAVIDSON, O., DE CONINCK, H. C., LOOS, M. & MEYER, L. 2005 *IPCC Special Report on Carbon Dioxide Capture and Storage*. Cambridge University Press.

NEUFELD, J. A., HESSE, M. A., RIAZ, A., HALLWORTH, M. A., TCHELEPI, H. A. & HUPPERT, H. E. 2010 Convective dissolution of carbon dioxide in saline aquifers. *Geophys. Res. Lett.* **37**, 22404.

NIELD, D. A. & BEJAN, A. 2006 *Convection in Porous media*, 3rd edn. Springer.

ORR, F. M Jr. 2009 Onshore geologic storage of CO_2. *Science* **325**, 1656–1658.

OTERO, J., DONTCHEVA, L. A., JOHNSTON, H., WORTHING, R. A., KURGANOV, A., PETROVA, G. & DOERING, C. R. 2004 High-Rayleigh-number convection in a fluid-saturated porous layer. *J. Fluid Mech.* **500**, 263–281.

PAU, G. S. H., BELL, J. B., PRUESS, K., ALMGREN, A. S., LIJEWSKI, M. J. & ZHANG, K. 2010 High-resolution simulation and characterization of density-driven flow in CO_2 storage in saline aquifers. *Adv. Water Resour.* **33**, 443–455.

RADKO, T. & SMITH, D. P. 2012 Equilibrium transport in double-diffusive convection. *J. Fluid Mech.* **692**, 5–27.

SLIM, A. C., BANDI, M. M., MILLER, J. C. & MAHADEVAN, L. 2013 Dissolution-driven convection in a Hele–Shaw cell. *Phys. Fluids* **25**, 024101.

STERN, M. E. 1969 Collective instability of salt fingers. *J. Fluid Mech.* **35**, 209–218.

WEN, B., CHINI, G. P., DIANATI, N. & DOERING, C. R. 2013 Computational approaches to aspect-ratio-dependent upper bounds and heat flux in porous medium convection. *Phys. Lett.* A (in press).

WEN, B., DIANATI, N., LUNASIN, E., CHINI, G. P. & DOERING, C. R. 2012 New upper bounds and reduced dynamical modelling for Rayleigh–Bénard convection in a fluid-saturated porous layer. *Commun. Nonlinear Sci. Numer. Simul.* **17**, 2191–2199.

WOODING, R. A., TYLER, S. W., WHITE, I. & ANDERSON, P. A. 1997 Convection in groundwater below an evapourating salt lake: 2. Evolution of fingers or plumes. *Water Resour. Res.* **33**, 1219–1228.